EUROFUSION WPMST1-PR(16) 15376

M Dunne et al.

Global performance enhancements via pedestal optimisation on ASDEX Upgrade

Preprint of Paper to be submitted for publication in
Plasma Physics and Controlled Fusion

This work has been carried out within the framework of the EUROfusion Consortium and has received funding from the Euratom research and training programme 2014-2018 under grant agreement No 633053. The views and opinions expressed herein do not necessarily reflect those of the European Commission.

Global performance enhancements via pedestal optimisation on ASDEX Upgrade

M.G. Dunne[1], L. Frassinetti[2], M.N.A. Beurskens[3], M. Cavedon[1,4], S. Fietz[1], R. Fischer[1], L. Giannone[1], G.T.A. Huijsmans[5], B. Kurzan[1], F. Laggner[6], P.J. McCarthy[7], R.M. McDermott[1], G. Tardini[1], E. Viezzer[1], M. Willensdorfer[1], E. Wolfrum[1], the EUROfusion MST1 Team[8], and the ASDEX Upgrade Team[1]

[1]Max-Planck-Institut für Plasmaphysik, Boltzmannstraße 2, D-85748 Garching,Germany
[2]Division of Fusion Plasma Physics, KTH Royal Institute of Technology, Stockholm
[3]Max-Planck-Institut für Plasmaphysik, D-17491 Greifswald,Germany
[4]Physik-Department E28, Technische Universität München, Garching Germany
[5]CEA, IRFM, 13108 Saint-Paul-Lez-Durance, France
[6]Institute of Applied Physics, TU Wien, Fusion@ÖAW, 1040 Vienna, Austria
[7]Physics Department, University College Cork, Cork, Ireland
[8] See http://www.euro-fusionscipub.org/mst1

E-mail: mike.dunne@ipp.mpg.de

Abstract. Results of experimental scans of heating power, plasma shape, and nitrogen content are presented, with a focus on global performance and pedestal alteration. In detailed scans at low triangularity, it is shown that the increase in stored energy due to nitrogen seeding stems mainly from the pedestal, with a small additional contribution from increased core density peaking. It is also shown that the confinement increase is driven through the temperature pedestal at the three heating power levels studied. In a triangularity scan, an orthogonal effect of shaping and seeding is observed, where increased plasma triangularity increases the pedestal density, while impurity seeding (carbon and nitrogen) increases the pedestal temperature in addition to this effect. Modelling of these effects was also undertaken, with interpretive and predictive models being employed. The interpretive analysis shows a general agreement of the experimental pedestals in separate power, shaping, and seeding scans with peeling-ballooning theory. Predictive analysis was used to isolate the individual effects, showing that the trends of additional heating power and increased triangularity can be recoverd. However, a simple change of the effective charge in the plasma cannot explain the observed levels of confinement improvement in the present models.

1. Introduction

Understanding the positive impact of impurity seeding on global confinement on ASDEX Upgrade (AUG)[1, 2], JET[3, 4], and Alcator C-Mod[5] has been the subject of many experiments and modelling attempts in recent years. This effect ranges in magnitude from a few percent in lower power AUG discharges, to up to 40%[2]. Several possible driving mechanisms have been proposed to determine this confinement improvement. Beurskens et al.[4] provide an overview of the three main possibilities; changes to the core stability, an edge peaked Z_{eff} profile, and changes to the pedestal stability. The first two do not fit with experimental evidence of, respectively, fixed core gradient lengths and measured impurity profiles which are observed to be either flat or have a pedestal.

One consistent observation on all of these devices is that the confinement improvement seems to originate in the pedestal. A detailed gyrokinetic analysis of one AUG discharge with impurity seeding found that the core gradient lengths were still clamped at the same critical gradient length by ITG turbulence[6]. For a different discharge, the edge electron temperature was observed to increase by 40%, leading via stiff profiles to an increase of the global confinement of the same order[2].

The use of impurity seeding to recover the apparent loss of confinement in baseline discharges between JET-C and JET-ILW conditions has also been studied in combination with a shape scan. In JET-C, it was routinely observed that increasing the plasma triangularity also increased confinement. This benefit was not found in the first JET-ILW baseline plasmas. However, when nitrogen was seeded the beneficial effect of plasma shaping on confinement was returned[4]. This effect is also not currently understood.

In order to understand these changes in the pedestal and to direct experiments, it is necessary to know what factors can influence the final pedestal. Peeling-ballooning theory[7] is currently thought to limit the peak pedestal performance prior to an ELM crash. It therefore provides the framework on which pedestal experiments can be based. This theory states that there is a critical combination of pedestal gradient, edge current density, and pedestal width which creates a linearly unstable coupled MHD mode, the peeling-ballooning mode. The peeling mode is driven by the edge current density while the ballooning mode is driven by the edge pressure gradient. The theory also predicts that there is not one specific gradient at which the pedestal becomes unstable; if the gradient is held constant but the width increases, the pedestal becomes more unstable. Of course, the ultimate parameter that is critical for predicting the performance of future fusion devices is the pedestal height, a combination of the gradient and the width, and so this is the main parameter of focus for confinement studies. The EPED model[8] has been developed as a combination of a turbulence limited pedestal gradient and peeling-ballooning limited pedestal height and is currently the most successful model for predicting pedestal heights.

This paper reports on a set of nitrogen seeded AUG experiments which were aimed at documenting the changes to the global and pedestal confinement over a range of

plasma beta, impurity content, and shapes. In particular, changes to the height of electron and ion temperature and electron density pedestals will be documented over the range of plasmas studied. Section 2 will describe the scenario set-up and the pedestal parameters. The effect of plasma shaping on confinement and its interaction with nitrogen seeding will be discussed in section 3. An initial stability analysis of the dataset with both interpretive and predictive stability codes will be presented in section 4 and a summary and discussion of the results will be presented in section 5.

2. Overview of nitrogen seeding

These experiments were designed to achieve a variation in plasma beta, plasma shape, and impurity content. A subset of the discharges is presented here (18 timeslices in total), namely with a constant plasma shape at medium triangularity ($\delta = 0.25$) and core line integrated density ($\sim 7.5 \times 10^{19} \mathrm{m}^{-2}$). Since the main focus of the paper is the interaction of global and pedestal confinement, discharges with prominent MHD activity (notably, 3/2 and 2/1 modes) were discarded from the analysis. Some 1/1 activity, either sawteeth or fishbones, was present in the majority of the discharges studied here. Discharges which featured pronounced detachment in the divertor, indicated by the measurement of the divertor temperature[9], were also excluded. A magnetic field of -2.5 T and plasma current of 1 MA were set for all discharges presented in this paper. A variation of global beta was achieved in the reference (no applied nitrogen seeding) discharges by varying the external heating power. In all discharges 1 MW of central electron cyclotron resonance heating (ECRH) heating was applied to prevent impurity accumulation. Additional neutral beam injection (NBI) powers of 5, 10, and 12.5 MW was also applied, with 2 MW of ion cyclotron resonance heating (ICRH) also applied at the highest NBI power level.

An overview of the normalised plasma parameters is shown in figure 1. $H_{98,y2}$, the thermal confinement time normalised to the ITER-98 scaling, is plotted as a function of (a): line integrated density and (b): β_N. The three symbol types correspond to the amount of heating applied in addition to the central ECRH. Red symbols denote discharges with no nitrogen seeding while blue symbols correspond to various levels of nitrogen seeding, giving the spread in stored energy. As mentioned, the density was kept constant for the lower triangularity discharges. A strong correlation between β_N and $H_{98,y2}$ can be seen within each of the heating power steps in figure 1(b); this is in fact a trivial result as only one parameter, the impurity content, which does not appear in the $H_{98,y2}$ scaling, was varied between discharges. In effect, $H_{98,y2}$ and β_N are both acting as the normalised plasma stored energy in this plot and such a trend is expected; this figure is shown only to present an overview of the operational space in these discharges. Operation above β_N=3 is experimentally difficult due to the onset of MHD activity such as resistive wall modes or neoclassical tearing modes; the highest confinement presented here is slightly below β_N=3.

The maximum improvement in confinement due to nitrogen seeding in these

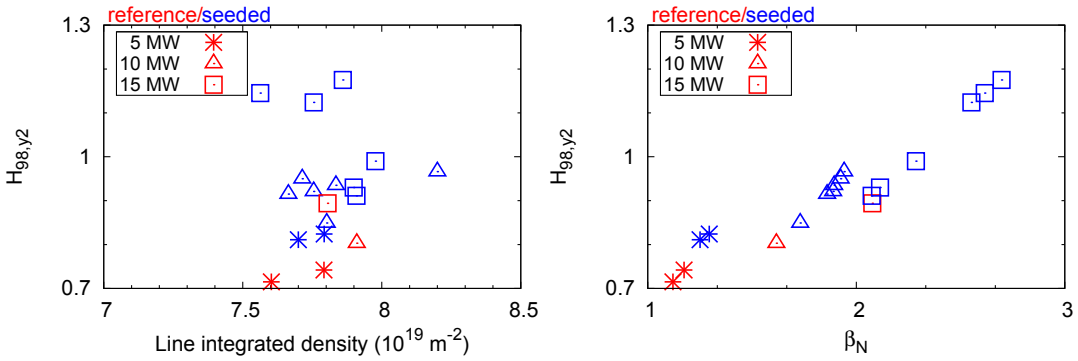

Figure 1. Existence diagram for the discharges presented in this section showing $H_{98,y2}$ as a function of (a) line integrated density and (b) normalised plasma beta. No trend with density is observed in the small density range covered, while an unsurprising trend with beta is seen; both $H_{98,y2}$ and β_N acting as measures for the thermal stored energy. Red symbols indicate reference discharges, blue symbols show their nitrogen seeded counterparts.

discharges (defined as $(W_{MHD,max} - W_{MHD,ref})/W_{MHD,ref}$) is 8%, 15%, and 25% in the low, medium, and high heating power cases, respectively. However, whether this is an effet of the global plasma beta or the nitrogen content is not immediately clear. At lower input power, the divertor goes more easily into detatchement due to radiation, meaning only a lower amount of nitrogen seeding can be applied. In order to make an estimate of the impact of beta on the allowed increase in confinement, the nitrogen content in the plasma must first be known.

Measurements of the impurity content are facilitated by the extensive set of charge exchange recombination spectroscopy (CXRS) diagnostics on AUG, with one core system and two high resolution systems focussed on the pedestal available[10]. These systems provide information on the ion temperature, impurity rotation, and impurity density profiles. To determine the nitrogen content in the plasma, the impurity density has been calculated from the measured intensities using the CHICA code. In addition to nitrogen, the concentrations of boron and carbon have been assumed to be constant at 0.5% each; these discharges were performed far away from a boronisation so a large boron fraction is not expected. The combination of the nitrogen measurement and assumptions on boron and carbon and quasineutrality allows the main ion density and Z_{eff} to be calculated. Following these assumptions and measurements Z_{eff} was observed to vary between 1.3 and 2.2 over the entire dataset, which is a reasonable range for ASDEX Upgrade.

The normalised confinement time is plotted as a function of Z_{eff} in figure 2. At each power step there is a clear increase in confinement at increased Z_{eff}. Although the figure shots a general trend of an increase at lower Z_{eff}, in particular for the 10 MW points, the ~15% uncertainty in the n_{imp} measurement makes a difinitive statement on this difficult. There is also one spurious point at $Z_{eff} = 2.1$; there does not appear to be anything unusual about this discharge, it however fails to reach the same confinement

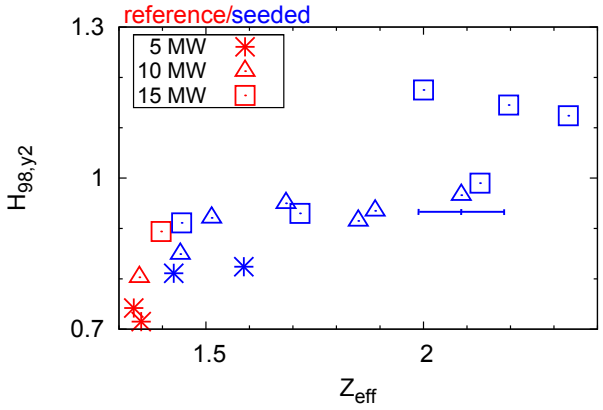

Figure 2. Confinement improvement factor $H_{98,y2}$ plotted as a function of Z_{eff} for the three heating powers in the low-/*delta* seeding scan. The confinement rises even at low Z_{eff} with increasing heating power and also as a function of Z_{eff} at each heating power level. An error bar, representing the uncertainty in the nitrogen density calculation is shown as the horizontal line below the highest Z_{eff} value at 10 MW. This corresponds to an uncertainty in the nitrogen density of ~15%.

as the other 15 MW discharges. Predictive pedestal analysis will examine the impact of Z_{eff} on the pedestal in section 4.4 and may be able to shed light on these observations.

Now that the confinement improvement due to nitrogen seeding has been characterised in basic terms, we take a look at how the global and pedestal profiles change in response to impurity seeding. AUG is equipped with an extensive set of electron and ion measurements. The electron temperature is measured via an electron cyclotron emission (ECE) system[11] and two Thomson Scattering (TS) systems[12, 13], one with a laser set aimed vertically through the core plasma and the second which probes the edge plasma. The electron density is also measured by these TS systems, plus a lithium beam emission spectroscopy (LiBES) diagnostic[14, 15] at the edge and five lines of a deuterium-cyanide-nitrogen (DCN) laser interferometry set-up[16] which provides integral information about the density profile. The ion temperature and density measurements have already been discussed.

Figure 3 shows the response of the global thermal profiles to nitrogen seeding; (a) shows the electron temperature profiles (circles) in a reference (red) and seeded phase (blue). The ion temperature profiles are shown as triangles with black indicating reference data and green showing the seeded data. A large response to impurity seeding is clear in both channels, beginning at the pedestal top and propagating into the core plasma via stiff profiles, consistent with previsous works. Figure 3(b) shows the electron and ion density profiles with the same symbol and colour coding as for the temperature profiles. No significant response can be seen in the global electron density profiles, although the nitrogen content is increased by a factor of ~3.

These measurements have been made for all discharges, allowing a detailed examination of the core and pedestal profile response to impurity seeding to be determined. The core plasma response will be analysed via the profile peaking of T_e,

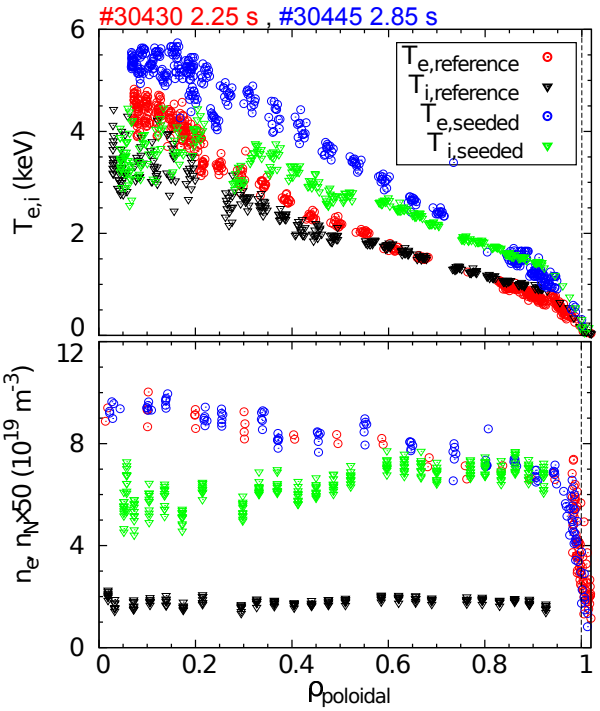

Figure 3. (a) electron (circles) and ion (triangles) temperature profile data during a reference (red,black) and nitrogen seeded (blue,green) phase. (b) electron density (circles) and nitrogen density (triangles,scaled $\times 50$) during the same phases. A strong increase both electron and ion temperature is evident, while the electron density shows no reaction.

T_i, and n_e. The profile peaking for this purpose is defined as $(a_{\rho_{pol}=0.5}/a_{\rho_{pol}=0.85})$, with a=$T_e$, T_i, n_e. The ion temperature is determined from the core CXRS diagnostic which covers the plasma radius out to ρ_{pol} 0.95. The peaking of the electron density and temperature are determined from the reconstruction of ECE and LiBES/DCN data via integrated data analysis (IDA)[17]. This models the electron temperature and density in a self consistent manner, allowing highly accurate profiles to be determined across the entire plasma radius. The profile peaking for these three parameters is shown as a function of beta in figure 4. Again, red points indicate the reference plasmas while blue points refer to seeded plasmas. This figure indicates that the electron temperature profiles are more peaked than the ion temperature profiles. This may be partially due to the use of ECRH heating in the core of these plasmas, though the peaking factor was taken in the outer half of the plasma, far outside of the deposition location of the ECRH. What is more important, however, is any change of the peaking factor when impurity seeding is applied to these plasmas. For both the electron and ion temperature profiles, the peaking factor within each power level is unchanged by impurity seeding.

Despite the peaking of the temperature profiles remaining essentially constant over the plasmas investigated, the density profile peaking changes continuously. No sudden jump is observed, but rather a gradual increase of the peaking from ~1 to ~1.4 is seen over the range of plasma beta, independent of whether nitrogen seeding is applied or not. This

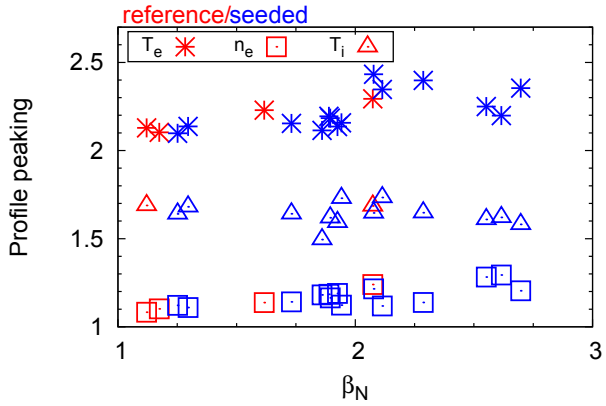

Figure 4. Profile peaking of electron temperature (stars), ion temperature (triangles), and electron density (squares) in the discharges from this dataset. Red symbols indicate reference datapoints while blue indicates nitrogen seeded datapoints.

effect can be well understood following the work of Angioni et al. on JET and AUG[18], where the impact of collisionality on density peaking was investigated. This work found an inverse correlation between density profile peaking and mid-radius collisionality on both machines; the collisionality was determined to be a more important factor than just the density. It was already shown in figure 1 that the line integrated density remains constant in these plasmas, indicating that the increased plasma beta comes from an increased temperature. This then corresponds to a decrease in the collisionality, resulting in the observed increased density profile peaking. The observation of constant gradient lengths of both ion and electron temperatures in these plasmas is a strong indication that the pedestal plays a critical role in confinement improvement via nitrogen seeding, which we will now investigate.

2.1. Pedestal top parameters

Since the principal goal of these experiments was to gain good pedestal measurements in impurity seeded scenarios, care was taken to set up the discharges in such a way that radial sweeps could be incorporated. These radial sweeps were of 400 ms duration and moved the plasma outwards by 1 cm in the first half and then back to its standard position in the second half. This increases the effective number of lines of sight of all the diagnostics and allows the pedestal structure to be determined with high accuracy on this timescale. In particular, an overlap of the edge and core TS diagnostics was important as this formed the basis of alignement of the other kinetic diagnostics; the ECE and LiBES diagnostics were aligned such that their respective profiles overlapped with the TS and the CXRS measurements were shifted such that the steep gradient region in both electron and ion temperature pedestals overlapped. Example edge data are shown in figure 5. The same timewindows and discharges as in figure 3 are shown, with the same symbol and colour coding (circles show electron profiles, red indicates reference data and blue indicates seeded data, black and green triangles show the corresponding

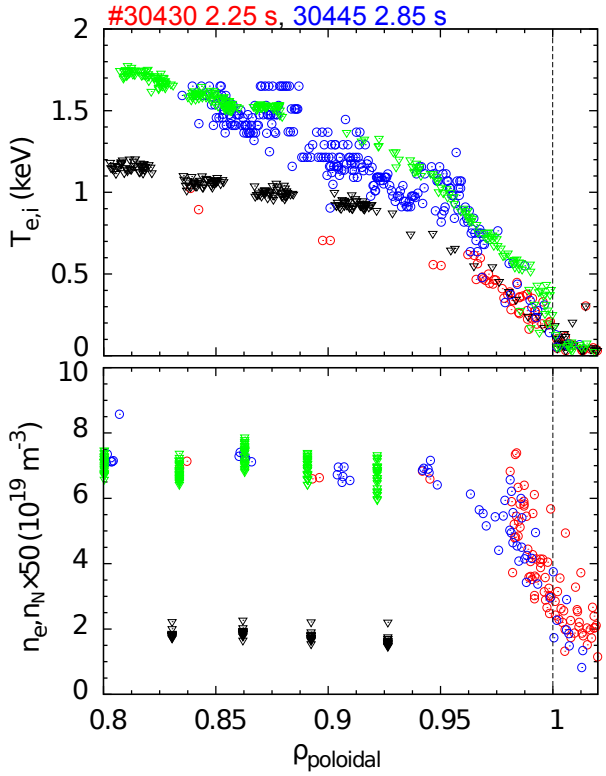

Figure 5. Edge (a) electron temperature and (b) density profiles in reference (red circles) and seeded (blue circles) phases (zoomed from data in figure 3. Corresponding ion temperature and nitrogen density data are shown as black and green triangles. As noted for the full profile in figure 3, the electron density profile shows little reaction to impurity seeding while the confinement improvement takes places in the pedestal temperature profiles.

ion temperature and nitrogen density data).

Each of the profiles used for the following analysis were constructed via a modified hyperbolic tangent (m-tanh) fit to a set of data averaged over a time window between 4 and 0.5 ms prior to an ELM crash in a 0.3 s time range during the discharge. This allows the critical pedestal before the ELM onset, or the largest achievable pedestal, to be analysed. In particular, the aim of this analysis is to document the changes in pedestal structure which may be due to an alteration of the peeling ballooning stability. Figure 6 shows beta as a function of (a) the density and (b) the temperature at the pedestal top.

As has already been shown, the total density of the plasma does not vary significantly in the database presented here. This is also reflected in the behaviour of the pedestal top, although there is a trend towards lower pedestal top densities at the highest beta level; nitrogen seeding appears to have no systematic effect on the pedestal top density. In contrast, the increase of beta is driven by a large increase in the pedestal top electron temperature, which increases by over a factor of two across the range of plasmas studied. This increase is approximately linear and does not appear to depend on whether the beta is increased by impurity seeding or additional input power. This

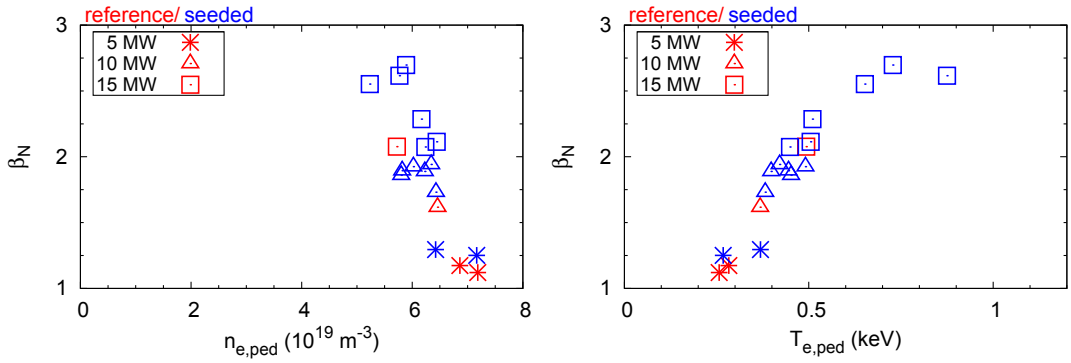

Figure 6. Global normalised beta as a function of (a) pedestal top density and (b) pedestal top temperature. There is a slight inverse trend of increasing beta with decreasing density, but the dominant factor in increasing beta (via either more input power or nitrogen seeding) is the pedestal top temperature.

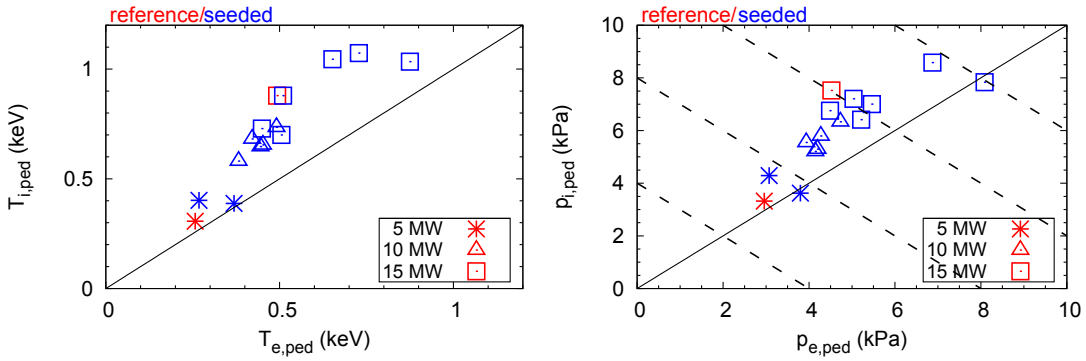

Figure 7. (a): pedestal top ion temperature plotted as a function of pedestal top electron temperature. (b): pedestal top ion pressure plotted as a function of pedestal top electron pressure. The solid lines in both figures denote equivalence; the dashed lines in (b) indicate lines of constant total pressure. Figure (b) shows that the total pedestal top pressure increases as beta is increased via either increased heating power or nitrogen seeding. Combined with the information from figure 6, it is clear that this increase is driven by both electron and ion pedestal temperatures.

behaviour, as well as the lack of change in profile peaking, implies once again that the pedestal and core are strongly linked.

Since it is difficult to envisage a mechanism whereby the core profile peaking would transiently increase, increasing beta and thus allowing an increase of the pedestal top, and then disappear, it seems clear, based on the current evidence, that the observed increase in confinement is stemming from the pedestal itself. One possibility which has been put forward is that the pedestal pressure remains constant, with a flat ion density profile diluted in the pedestal while the ion temperature profile is allowed to rise in the core due to stiff gradient lengths. If this were the case, one would expect that the ion temperature rises significantly as seeding is applied. To test this, the ion temperature is plotted as a function of the electron temperature in figure 7(a).

Here, we see that the ion temperature pedestal is indeed higher than the pedestal top electron temperature; the solid line indicates equivalence between electron and ion temperatures. However, in this dataset, the ion temperature pedestal appears to be wider than the electron temperature pedestal, but to have a similar gradient. When the values of T_i and T_e are compared at the location of the electron temperature pedestal top, they match quite well. At a first glance, one might assume that this is, indeed, evidence for the dominant effect of impurity dilution on confinement (assuming that the electron and ion heat fluxes should match near the pedestal top). However, there are issues with this; 7(a) shows no difference in the increase of $T_{i,ped}$ and $T_{e,ped}$ if impurities are seeded or not. A more clear indication that this is not the case arises when one calculates the ion pressure at the pedestal top according to the combination of measurement and assumptions used for the calculation of Z_{eff}. This has been done for the current database set and the results are plotted as a function of the electron pressure at the pedestal top in figure 7(b).

The solid line in this case indicates equivalence between p_e and p_i while the dashed lines are lines of constant total pressure at the pedestal top. The measurements indicate that the ion pressure does increase more than the electron pressure, but show that this is, again, independent of whether impurities are seeded or not. In addition, at no point is the total pressure at the pedestal top conserved; it always increases, either with applied heating power or with impurity seeding. While this is not a surprising result, it provides a clear indication that the stability of the pedestal must change in some manner with impurity seeding. It is therefore interesting to combine these experiments with other well known pedestal modification effects, such as plasma shaping.

3. Effect of plasma shaping

Within the framework of peeling-ballooning theory, plasma shaping alters the shape of the peeling-ballooning boundary, allowing access to a region of higher pressure gradient and current density. Higher confinement in high triangularity discharges was a typical observation in the JET-C device[19, 4]. In the JET-ILW device this benefit was initially lost, meaning that confinement at both low and high triangularity was the same[4, 20]. When nitrogen is seeded in JET-ILW confinement increases by ~15% in low triangularity discharges and by ~40% in high triangularity discharges[20]. To see if this difference in the effect of nitrogen could also be observed in AUG, a beta scan was also performed in a high triangularity shape, with and without nitrogen seeding. Three power levels with 5, 7.5, and 10 MW of NBI heating power were used. Operation with 15 MW at high triangularity and nitrogen seeding was also attempted, but the resulting plasma had a normalised beta of 3.3, causing the onset of a large NTM and as such is not presented here.

A comparison of the shapes is shown in figure 8. The shape was designed such that the lower triangularity and strikepoints, as well as the outer plasma radius, were kept as similar as possible. The stronger shaping was then effected at the upper portion of the

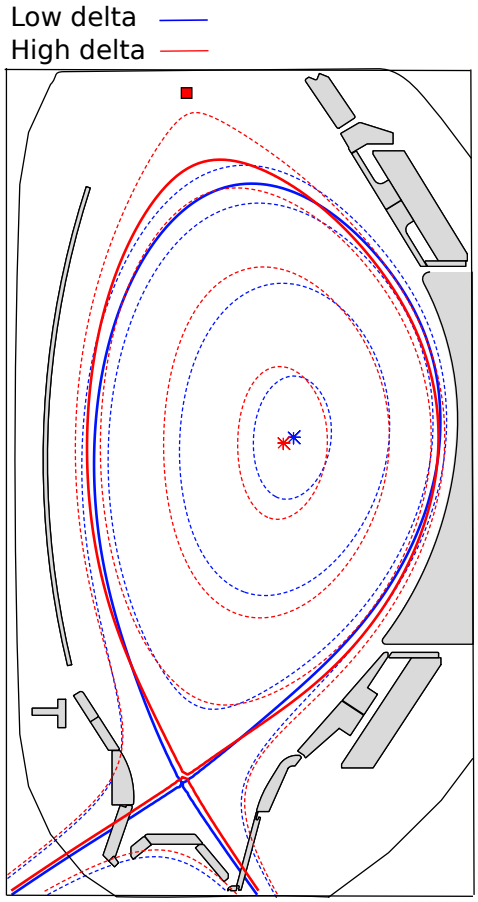

Figure 8. Comparison of the low (red) and high (blue) triangularity shapes used in this study.

plasma, where both triangularity and elongation were increased. Higher triangularity can be reached in ASDEX Upgrade; this was not done in this case as it was also desired to keep the elongation as similar as possible, as this can also have a strong effect on the plasma performance.

The discharges used in the shape scan had two phases, one for low triangularity and one for high. This allows a direct comparison of the performance in the two shapes in the same machine conditions. Nitrogen was seeded in successive discharges. Only one level of nitrogen was used for most of the power levels as the nitrogen level scan had already been done at low triangularity. In these cases, the most effective nitrogen level from this scan was taken. An example timetrace of discharge #30476 is shown in figure 9, where box (a) shows the heating power, which is kept constant, (b) shows the gas fuelling rates, (c) shows the average triangularity, (d) shows the density, (e) shows the normalised plasma beta, and (f) shows the ELM frequency.

Stronger plasma shaping has two main effects on the plasma performance. As shown in figure 9, the density increases from a line integrated value of 8 to 11, with the global beta also increasing by a similar percentage. The radiated power does not change significantly as triangularity is increased. In addition to the density increase, the

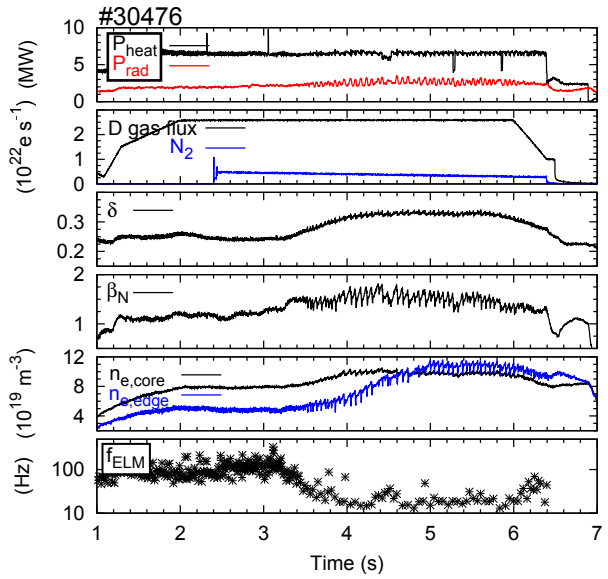

Figure 9. Timetraces of (a) heating (black) and radiated (red) power, (b) deuterium (black) and nitrogen (blue) fuelling rates, (c) average triangularity, (d) normalised plasma beta, (e) edge (blue) and core (black) line integrated densities, and (f) ELM frequency. Stronger plasma shaping has a positive impact on the stored energy, but reduces the ELM frequency significantly, leading to much larger individual ELM events.

ELM frequency decreases by almost one order of magnitude when the higher shaping is reached. The individual ELM events also become clear to see in timetrace of the plasma beta and the line integrated densities with ~20% of the plasma stored energy lost at each ELM crash. It cannot be determined from the current database of discharges if the decrease of ELM frequency is due soley to the change in plasma shape or if the increased plasma density plays a role. The ELMs themselves will not be discussed in detail in this paper and are the subject of accompanying work.

The confinement for the three power levels in low and high triangularity, with and without nitrogen seeding is shown in figure 10. The circles show the low triangularity phases and the triangles show the high triangularity phases. As before, red shows unseeded plasmas, blue shows seeded plasmas. Empty shapes indicate the 5 MW plasmas, partially filled shapes the 7.5 MW plasmas, and fully filled shapes the 10 MW plasmas. Also shown in these figures are results from a 10 MW plasma which was seeded with CD_4 (black points). A more detailed comparison of the three 10 MW plasmas (reference, nitrogen seeded, and CD4 seeded) will be shown in an accompanying paper[21]. The trend is as expected; increased plasma shaping increases confinement, even at low beta (in contrast with results from JET-ILW where only higher power discharges in JET-ILW have shown improved confinement with plasma shaping[22]). The plot confirms that the increased confinement at high triangularity is driven by a density increase at each power level. A clearer picture of the confinement improvement mechanisms in this discharge set emerges when one looks at the electron temperature and density near the pedestal top. Near the pedestal top in this case means at $\rho_{\mathrm{poloidal}} = 0.95$;

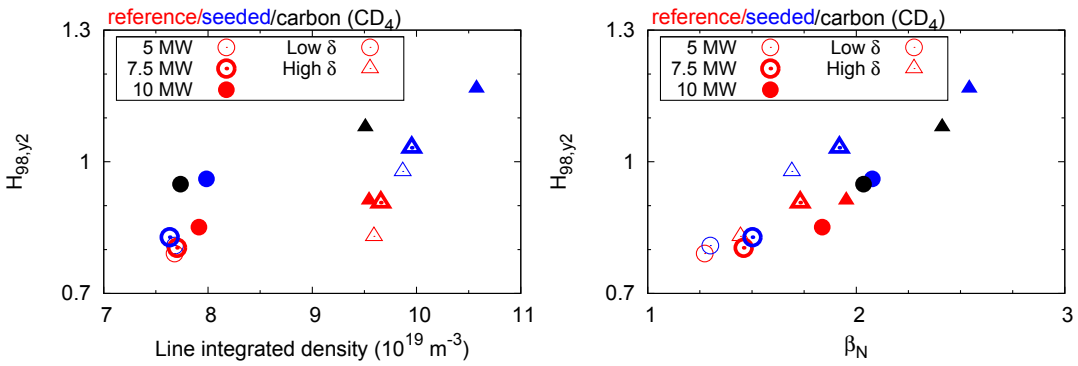

Figure 10. (a) H98y2 as a function of line integrated density. Circles and triangles indicate low and high triangularity plasmas, respectively, red indicates reference plasmas, blue shows their seeded counterparts. The three power levels used in the experiment are shown by empty symbols (5 MW), partially filled symbols (7.5 MW), and filled symbols (10 MW). (b) H98y2 plotted against beta normalised, showing a similar trend as has already been discussed in section 2.

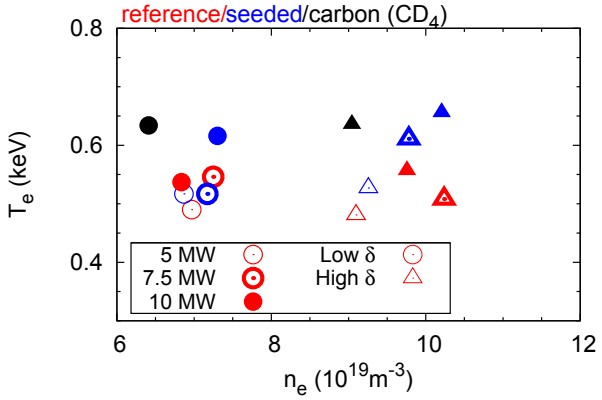

Figure 11. Electron temperature and density values at $\rho_{\mathrm{poloidal}} = 0.95$ for the low and high triangularity comparison discharges. The colour and symbol code is the same as in figure 10. There is a clear separation of the effect of plasma shaping (only density), and impurity seeding (only temperature, indicating that different physical mechanisms are dominant for each effect.

this was chosen as it represents the changes the profiles undergo at high triangularity better than the fitted pedestal top values. This is mainly an issue for the temperature profiles as the ECE diagnostic was in cutoff at the high densities encountered. Figure 11 shows the temperature and density values at $\rho_{\mathrm{poloidal}} = 0.95$ with the same colour and symbol coding as figure 10.

The most striking feature of this figure is the strong separation of pedestal top density between low and high triangularity; this was already indicated in the overview figure 10 and is highlighted here again. Increasing the plasma shape seems to have no impact at all on the pedestal top temperature. Conversely, impurity seeding only increases the pedestal top temperature (if it has any impact). This is seen most clearly for the 10 MW data points (filled symbols); impurity seeding, either wtih nitrogen or

CD_4, increases the pedestal top temperature by ~15%, while the shaping increases the pedestal top density by ~40%. There is one data point which does not follow this trend. In the 7.5 MW pulse, nitrogen has a limited effect on the pedestal top at low triangularity, while at high triangularity the pedestal top temperature is increased by almost 10%. This is an interesting contrast to the effect seen at JET, where triangularity has no effect until impurity seeding is applied. However, as has already been pointed out, there is a general trend that the confinement improvement with nitrogen seeding is greater at higher beta; this particular discharge may be a more solid proof of this. To verify this, a complete understanding of the effect of nitrogen seeding on the pedestal is required. This is, at the moment, lacking, but with the current data set we can now start investigating the various hypotheses with the aid of interpretive and predictive pedestal models, as will be discussed in the next section.

4. Stability analysis

The stability of several of these plasmas was analysed using a combination of equilibrium tools available at AUG and the ITM j-alpha workflow[23] in combination with the HELENA fixed-boundary equilibrium solver[24], which was used to modify the experimental profiles to construct a grid of points in stability space. Using the MISHKA-fast linear stability code[25], the stability of each point in this grid was evaluated to determine the location of the stability boundary. The workflow for this analysis is outlined in the following: first, the raw kinetic data, as described in the sections above, were used as a constraint on the pressure profile in the CLISTE equilibrium code[26, 27]. Magnetic and SOL current data were taken from the same time ranges and windows relative to the ELM crashes as the kinetic data[28]. The plasma boundary was then modified to remove the x-point by cutting the plasma at a particular radial location in flux space to avoid the x-point singularity. The radial p' and ff' profiles were also cut at the same point, i.e. they were not squeezed into the reduced plasma volume. The choice of this cut-off parameter does have an impact on the calculated stability boundary, making it something of a nuisance parameter. However, in this work we are particularly interested in observing trends with the stability codes, rather than an exact quantitative determination of the pedestal stability, meaning a constant offset of the boundary is not so important to the results which will be presented in this section.

The CLISTE equilibria were then passed to the HELENA equilibrium solver for further refinement and translation to field-aligned coordinates. Once these "reference" equilibria have been constructed, the pressure and current density profiles were modified by the ITM j-alpha actor. The total beta and plasma current were kept constant during this operation; this means that the core profiles were increased (decreased) as the pedestal values were decreased (increased). The elements changed to alter the stability were the pressure gradient, via the pedestal height at a constant pedestal width, and the peak height of the edge current density, again at constant width and separatrix current density. A j-alpha grid consisting of 10x10 equilibria was used, with a step

size of 10% between each value of the pressure gradient and current density to provide enough resolution to accurately determine the location of the stability boundary. A critical growth rate for determining the boundary location was set at $0.04\gamma_{\mathrm{Alfven}}$.

The stability of each of these equilibria to a range of modes ($1 < n < 70$) was tested by using the MISHKA-fast stability code, which is a variant of the MISHKA-1 solver[25], solving a reduced set of the ideal MHD equations. The MISHKA-fast variant allows for a radially varying range of poloidal mode numbers, which greatly reduces the computational effort involved in analysing higher toroidal mode numbers. In particular, this facilitates the expansion of the peeling-ballooning stability boundary to the very low current density regime, which is particularly important for the low beta discharges analysed in this work. This means that both the peeling- and ballooning-dominated boundaries could be observed as well as the turning point, or nose, of the peeling-ballooning diagram which is pulled out at high plasma shaping, allowing access to higher confinement. Three particular stability studies were undertaken with the data presented so far in this paper: a beta scan, a shape scan, and the impact of nitrogen seeding. The results of the analysis and inividual conclusions are shown in the subsections below.

4.1. Beta scan

The three separate power levels without nitrogen seeding from the low triangularity database were chosen for analysis here. Data were taken over a 200 ms time window centered around 3.1 s in the shots #30472 (5 MW NBI), #30513 (10 MW NBI), and 2.1 s in discharge #30430 (15 MW NBI+ICRH). All shots also featured additional central ECRH of 1.5 MW. A radial scan of the plasma was used to cover the entire pedestal region with the diagnostics. The density is similar in all three cases, while both electron and ion temperatures at the pedestal top increase with more external heating power, as already discussed in section 2.

A comparison of the stability boundaries and operational points for each of the three cases is shown in figure 12. The symbols refer to the operational points in the pre-ELM phase for each of the discharges, while the solid lines show the calculated stability boundaries. In all cases, the operational points do not meet the peeling-ballooning boundary, indicating that there is an uncertainty in either the measurements or the theory, or a combination of both. The dashed lines in figure 12 give an estimate of this uncertainty by scaling the pressure gradient of the stability boundary down by 15% in all cases. At this reduced stability boundary, the agreement between theory and experiment is excellent. A 15% uncertainty in the stability boundary can be easily explained as a combination of uncertainty in the measured pedestal gradients, the 'cut-off' parameter which was discussed at the beginning of this section, and the absolute position of the pressure profile. Thus, the important point to take from this analysis is that the pedestals in this set of experiments can be described as being compatible with peeling-ballooning theory, and that the measured increase of the pedestal top and gradients is also predicted by the theory. The observed shift of the stability boundary

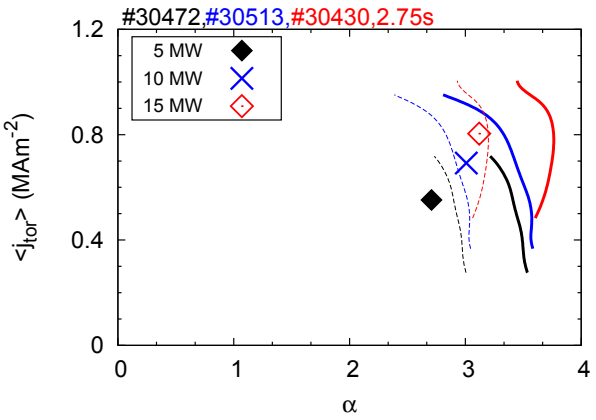

Figure 12. Operational points (symbols) and calculated stability boundaries (solid lines) calculated for discharges 30472 (filled diamond, black), 30513 (cross, blue), and 30430 (empty diamond, red). Also shown with the same colouring scheme but in dashed lines are the stability boundaries with the pressure gradient reduced by 15%, which the authors consider to be an acceptable magnitude for the combination of uncertainty in the data and model. The trend of increasing pedestal top with increasing external heating is reproduced.

to higher pressure gradients at higher input power is explained by an increased global shafranov shift, and hence local shear; this acts to stabilise ballooning modes, leading to the observed effect.

4.2. Shape scan

The discharge used for the shape scan was AUG discharge #30513, which had both a low and high triangularity phase at 10 MW of NBI power. The confinement improvement with shaping was discussed in section 3 and was observed to orignate with an increase of the density pedestal. The stability diagrams from the two phases of this discharge are shown in figure 13. Red shows the low triangularity phase and green shows the high triangularity phase. The diamonds indicate the relevant operational points. When the plasma shape is increased, the shape of the peeling-ballooning boundary changes, with the "nose" extending towards higher pressure gradients. Correspondingly, the operational point is allowed to move in this direction, increasing the total stored energy in the plasma. This explains the offset of the entire stability boundary in the high triangularity phase; the effect of beta and shaping cannot be easily experimentally separated.

There is an exception for the JET baseline plasmas during ILW operation, where the confinement is not increased with shaping. However, there is one important difference to note when comparing the JET scenario to the discharge presented here. The AUG discharge is already located near the nose of the diagram, in the region where the confinement benefit is going to be maximised. Stability calculations performed for JET have shown that, in contrast with the starting point in the AUG experiments, the JET-ILW baseline plasmas begin at a low beta and are located on the ballooning-dominated

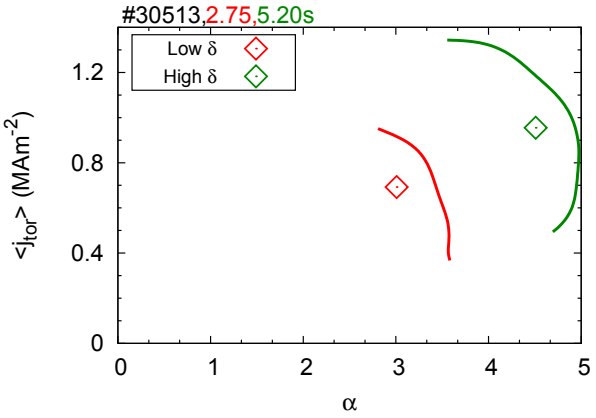

Figure 13. Combined stability diagrams for low (red) and high (green) triangularity phases of discharge #30513. The low triangularity stability boundary has a typical shape for AUG discharges, while the "nose" of the diagram is pulled out at high triangularity, allowing the higher pressure gradient and current density from this discharge.

(low current) part of the peeling-ballooning diagram. In the basic interpretation of the impact of triangularity on pedestal height and plasma confinement, this is not a region where any change of the pedestal with triangularity would be exected. This is one notable difference between this set of seeding experiments on AUG when comparing with recent results from JET; it is likely, given the results presented here, that there is not a different effect of nitrogen on confinement in either high or low triangularity. Rather, nitrogen seeding lifts the pedestal into a region where confinement can be further improved by triangularity. In order to make a definitive statement on this, predictive modelling of the pedestal is required such that the impact of the separate variables (plasma shape, impurity content, and density) on the final state can be determined.

4.3. Impurity seeded analysis

The impact of nitrogen seeding on the stability boundary was tested in two separate discharge scenarios, one each at low and high triangularity. The high triangularity phases of discharges #30507 (reference,red), #30513 (nitrogen seeded, blue), and #30518 (CD_4 seeded, black) were chosen for this analysis. In these shots, impurity seeding increased the confinement by ~15% by increasing the temperature pedestal top; the pedestal top values can be found in figure 11 and more detailed profile analysis for these discharges has been presented by Beurskens et al. [21].

The results of the detailed stability analysis for these three discharges is shown in figure 14. The diamonds indicate the experimental points, while the lines show the stability boundaries for the reference (red), nitrogen seeded (blue), and CD_4 (black) seeded discharges. The analysis shows that, indeed, the stability boundary is shifted to slightly higher pressure gradients (less than 10%) when impurity seeding is applied. However, the carbon boundary is even further away than the nitrogen boundary, despite

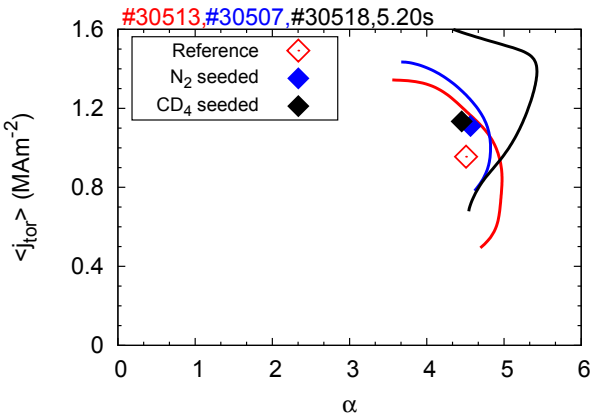

Figure 14. Stability boundaries and experimental points for the high triangularity phases of #30507 (reference,red), #30513 (nitrogen seeded, blue), and #30518 (CD_4 seeded, black). Despite the similar pedestals in the N and CD_4 seeded discharges, the boundary in the CD_4 case is shifted to higher pressure gradient; this indicates a ~10% uncertainty in the boundary location, consistent with the results from the beta scan.

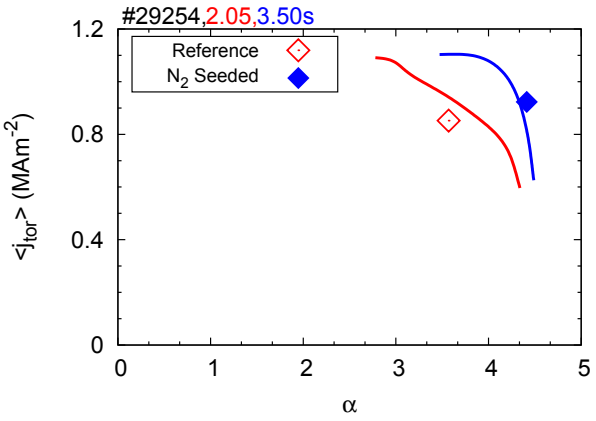

Figure 15. Stability of discharge #29254 for reference (red) and nitrogen seeded (blue) timepoints, showing a clear shift of the stability boundary to higher pressure gradient with the application of nitrogen seeding.

the two discharges having similar pedestal top values and gradients; this difference is approximately 10%, indicating that this is an approximate uncertainty in the boundary location (assuming similar discharge parameters). This is also consistent with the estimate of uncertainty in the boundary location in the beta scan in section 4.1

The second comparison was made using data from discharge #29254, in which pedestal pressure and current density profiles have previously been analysed[29] and which has the highest level of confinement improvement due to nitrogen seeding in AUG[2] at a 40% increase. This discharge was chosen since the effect on the stability of the pedestal should be very clear, due to the large changes in global and pedestal confinement. The stability boundaries for the reference and seeded timepoints during this discharge are shown in red and blue, respectively, in figure 15. In this case there is a large noticable difference in the stability boundaries when nitrogen seeding is

applied, which is outside of the uncertainties of the analysis, indicating that the stability boundary does indeed shift to higher pressure gradients. The experimental pressure gradient has increased significantly, while the current density has remained the same. Both points lie approximately on the stability boundary, supporting the hypothesis that it is indeed the pedestal stability which changes with nitrogen seeding in some way. The shift of the stability boundary towards higher pressure gradients is likely to be due to the increased plasma beta, which stabilises ballooning modes. This allows us to construct a basic model of how impurity seeding could lead to improved confinement. Since impurity seeding alone (without an increase in the pedestal stability) would act to decrease the current density, the operational point would slide along the negative slope of the stability boundary in j-alpha space, allowing access to higher pressure gradients. This improvment could then propagate into the core plasma, increasing the global beta and acting to further stabilise the pedestal in a bootstrapping effect which would terminate with a new balance of core heat transport and edge stability. Testing this hypothesis requires a predictive model for pedestal stability in which the various changes in the plasma (the increased Z_{eff} and global beta) can be separated in order to understand their relative contributions to the final observed state in figure 15.

4.4. Predictive analysis

A predictive pedestal model, such as the EPED1.0 model[30], requires two constraints: one on the pedestal height, and another on the pedestal gradient, or width. To this end, a routine was used to create temperature and density profiles in the same manner as the EPED1.0 model[30]. This means that a constant pedestal top density was set and the pedestal top temperature was varied. The pedestal width was set to be $0.11\times\sqrt{\beta_{\mathrm{pol,ped}}}$, which also defines the pedestal gradient for a given pedestal top pressure. Note that we have used here a larger value of this prefactor than typically used in EPED; it has previously been remarked for AUG that, while the pedestal width is consistent with the $\sqrt{\beta_{\mathrm{pol,ped}}}$ dependence, a slighly larger prefactor fits the data better[31]. In any case, this simply makes a linear shift of the predicted pedestal top and has no impact on the trends reported here. The core density profile was kept fixed while the temperature profile was varied such that the global beta used as an input was kept constant.

T_i was assumed to be the same as T_e (which is not the case in this set of experiments, but is sufficient for analysis of trends), and n_i was calculated by assuming boron and carbon as impurity species. Using these kinetic profiles, the neoclassical current, containing both bootstrap and Ohmic compenents, was calculated. The toroidal electric field, which is a required input for the calculation of the Ohmic component of the neoclassical current was calculated by assuming only neoclassical bootstrap current as non-inductive current and neoclassical resistivity and solving for a constant electric field to make up the provided plasma current.

To apply this analysis to the discharges performed here, the plasma current and magnetic field were set to 1 MA and 2.5 T respectively. The pedestal top density was

kept constant at 7e19 m-3. The two plasma shapes from figure 8 were chosen to examine the effect of low and high triangularity on the pedestal. The global plasma normalised beta was varied between 1 and 3 and two values of Z_{eff} were chosen at 1.3 and 2, resulting in 20 plasma scenarios to analyse. Example pressure and current density profiles for a low triangularity discharge with a β_N of 1.5 are shown in figure 16. The different colours show different pedestal top temperature values (and hence pedestal widths). The inset zooms in on the pedestal region showing how the pedestal top pressure and pressure gradient changes as well as the variation in edge current. The pedestal top temperature was evenly distributed between 300 and 1200 eV, encompassing the expected range of AUG operating conditions. As expected, the on-axis pressure varies significantly due to the global beta constraint. This is also the case for the current density, where internal inductance effects on the current density profile were not taken into account; the core current density profile has little effect on the edge stability in any case.

The MISHKA-fast code was used to determine the edge stability in all of these cases, and a critical growth rate of $0.04\gamma_{Alfven}$ was chosen to determine the stability boundary. The pedestal top value was determined from a linear interpolation between the value with the lowest growthrate above $0.04\gamma_{Alfven}$ and assuming that the next lowest pedestal top had a growth rate of 0. The results from these three scans are shown in figure 17. Shown as red and blue solid lines are the predicted pedestal top values for the low and high triangularity shapes, respectively, with a Z_{eff} of 1.3. Both of these scans show a general increase of the pedestal top with increasing global plasma beta. This has already been shown from the experiment and is also consistent with the interpretive stability analysis using the experimental data. In contrast with results from JET-ILW experiments, neither experiment or theory applied to these AUG shots shows a regime in which changing the plasma shape should not have an effect on the pedestal confinement. Scans were also conducted at a lower q value, corresponding to the ITER baseline scenario experiments conducted on JET, as well as at higher and lower density, none of which have yet yielded such a parameter regime on AUG.

The results from the scans with increased Z_{eff} are shown as the dashed lines for each of the beta points scanned. At low beta in the low trianguarity shape, the model predicts a slight degradation of the confinement, while at higher beta an increase is predicted. An increase is always predicted for the high triangularity case, indicating that the positive effect of impurity seeding may be limited to plasmas with pedestal top values above 14 kPa, which is not seen in the experiment; even at the lowest β_N of 1.2 a confinement increase with nitrogen was observed. A second problem arises with the magnitude of this effect. While this intially looks like a promising result, the predicted increase of the pedestal top is only ~1 kPa, meaning approximately 5% at the higher levels of beta. This contrasts strongly with the experiment where values between 25 and 40 % have been observed. Thus, while there is a positive effect of only an increased Z_{eff} on pedestal (and hence global) confinement, it is clear that other effects must also be taken into account in order to fully explain the experimental observations.

Other effects which can be taken into account are, for example, changes of the

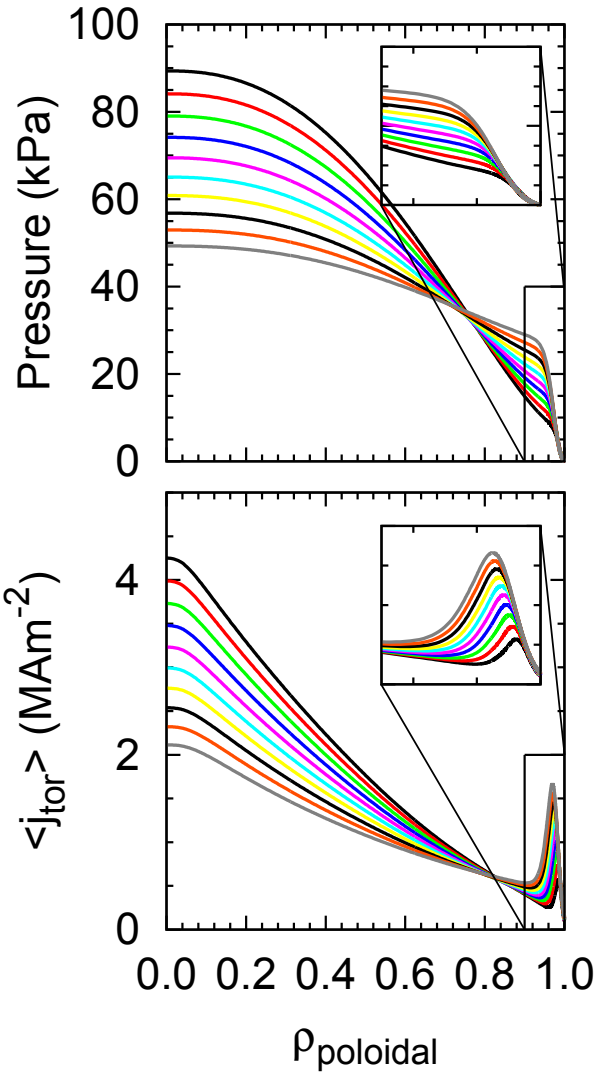

Figure 16. (a) pressure profiles and (b) current density profiles used as input for predictive stability calculations. Inset in both: pedestal region profiles in the range $0.9 < \rho_{\mathrm{poloidal}} < 1.0$.

separatrix temperature or density due to impurity seeding[32], which will impact the relative contribution of the respective gradients to the bootstrap current. However, the challenge lies in including these effects in a manner which is physically realistic. An altered separatrix temperature can be included in one of two ways; either the profile can be shifted radially inwards, which will move the gradient away from the separatrix and hence increase the confinement, or the temperature used for the base of the tanh fit can be decreased, which would lead to an increased gradient for the same pedestal top and width and hence decrease the predicted pedestal top pressure. A further effect is also an effective inward radial shift of the density profiles with nitrogen seeding which observed in the profiles presented in this paper[33]. An inward movement of the pressure gradient relative to the separatrix has a stabilising effect on the pedestal, leading to higher pedestal top pressures[34]; this effect will be presented in a future paper. While

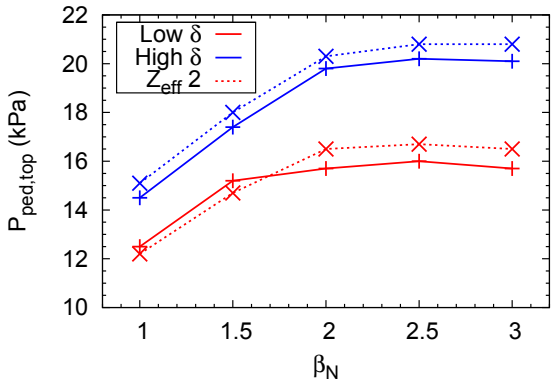

Figure 17. Predicted pedestal top values as a function of beta normalised in low (red) and high (blue) triangularity for $Z_{eff} = 1.3$ (solid lines) and 2.0 (dashed lines). A general increase of the pedestal top with increased beta is seen, while a stronger plasma shape has a very large effect on pedestal stability.

experimental observations can be included into the model for present-day devices, these uncertainties make the prediction of the ITER pedestal a challenge. A more complete understanding of the SOL-pedestal interaction and the boundary conditions which the SOL sets for the pedestal is thus urgently required in order to make more firm statements for ITER.

5. Conclusions

To summarise the observations, a series of experiments have been carried out on AUG to characterise the impact of impurity seeding on confinement. Nitrogen has been shown to have a beneficial effect on plasma confinement across a range of heating powers and plasma shapes, though the effect appears to be stronger at higher beta. It was shown that both nitrogen seeding and heating power act to increase the pedestal top temperature while having little effect on the density, and that the ion temperature was observed to increase more than the electron temperature. If we consider the ELM cycle and the fact that the electron density and temperature have been observed to increase at different rates after the ELM crash[35], it is a simple extension that the electron and ion temperatures also increase at different rates according to their respective heat fluxes in the outer plasma. An analysis by Sommer et al.[36] showed that, over a range of heating schemes at AUG, the ion heat flux at the pedestal top was significantly higher than the electron heat flux, lending support to this argument. Then, the ion temperature pedestal would simply heat up at a faster rate than the electron temperature pedestal over the ELM cycle, leading to these observations.

A triangularity scan was also presented. In this set of experiments, increased plasma shaping was always observed to increase the confinement. Furthermore, this was also correlated with an increase in the density pedestal. When nitrogen was included in the triangularity scan, a clear separation of the density and temperature responses to

shaping and seeding was observed; shaping impacts the density pedestal while impurity seeding increases the temperature pedestal. In one discharge, the impact of nitrogen seeding was only observed at high triangularity, but still on the temperature pedestal. Combined with the contrasting results at JET, this creates a picture where there is no intrinsic link between seeding and shaping, but rather that the separate effects can act to move the pedestal into a regime which is more receptive to, in the AUG case, a confinement benefit from impurity seeding.

Interpretive stability analysis of the beta and shape scans shows a qualitative understanding of these effects on the pedestal. Increased core heating leads to a stabilisation of the pedestal at lower pressure gradients while increased plasma shaping alters the shape of the peeling-ballooning boundary. In cases where the impact of nitrogen is 15%, the analysis does not show consistent results. However, in cases of large changes in the measured profiles and gradients, the analysis shows a clear trend; the stability boundary shifts to higher pressure gradients with impurity seeding and the associated increased global beta. Predictive analysis starting from a reference scenario and increasing the plasma beta and shape shows the same qualitative trends. However, when the plasma impurity content is changed, the model predicts only a small increase in the pedestal top, and even predicts a decrease at low beta, which is not observed in the experiments. It is clear that other effects will need to be taken into account in order to determine the mechanism of confinement improvement due to nitrogen seeding.

The question still remains; what other effects should be taken into account? Since the core plasma has been exlcuded in this and multiple other studies as a driving force behind the confinement improvement, and predictive analysis has ruled out the pedestal impurity content as being the sole driving force, it seems apparent that the SOL plasma must be analysed in more detail. At the very least, a qualitative understanding of how the upstream separatrix temprature and density profiles react to nitrogen seeding and its radiation pattern is required to provide more input to these models. In order to extrapolate these findings to ITER, a quantitative understanding is required. Experimentally, it should be possible to separate SOL radiation effects from pedestal impurity content effects by using a matrix of gases, such as nitrogen, neon, helium, and methane, for example, and scanning Z_{eff}. One possible effect is the impact of flux surface impurity asymmetries[37] on pedestal stability; measurements on Alcator C-Mod and AUG show an increased impurity density on the HFS, which would lead to a flux-surface averaged edge peaked Z_{eff} profile. It is not clear what effect this effect might have on stability, since the peaking occurs on the HFS, where the ballooning amplitude is lowest, but changes to the asymmetry factor with impurity seeding should also be investigated. Finally, the modelling of the experimentally observed inward shift of the density profile with nitrogen seeding, its link with SOL observations, and the corresponding increase of the pedestal top will be presented in a future paper.

Acknowledgement

This work has been carried out within the framework of the EUROfusion Consortium and has received funding from the Euratom research and training programme 2014-2018 under grant agreement No 633053. The views and opinions expressed herein do not necessarily reflect those of the European Commission.

References

[1] J. Schweinzer, A.C.C. Sips, G. Tardini, P.A. Schneider, R. Fischer, J.C. Fuchs, O. Gruber, J. Hobirk, A. Kallenbach, R.M. McDermott, R. Neu, T. Pütterich, S.K. Rathgeber, J. Stober, and J. Vicente. Confinement of improved H-modes in the all-tungsten ASDEX Upgrade with nitrogen seeding. *Nuclear Fusion*, 51(11):113003, November 2011.

[2] A. Kallenbach, M. Bernert, R. Dux, L. Casali, T. Eich, L. Giannone, A. Herrmann, R. McDermott, A. Mlynek, H.W. Müller, F. Reimold, J. Schweinzer, M. Sertoli, G. Tardini, W. Treutterer, E. Viezzer, R. Wenninger, and M. Wischmeier. Impurity seeding for tokamak power exhaust: from present devices via ITER to DEMO. *Plasma Physics and Controlled Fusion*, 55(12):124041, December 2013.

[3] C. Giroud, G. Maddison, K. McCormick, M.N.a. Beurskens, S. Brezinsek, S. Devaux, T. Eich, L. Frassinetti, W. Fundamenski, M. Groth, a. Huber, S. Jachmich, a. Järvinen, a. Kallenbach, K. Krieger, D. Moulton, S. Saarelma, H. Thomsen, S. Wiesen, a. Alonso, B. Alper, G. Arnoux, P. Belo, a. Boboc, a. Brett, M. Brix, I. Coffey, E. de la Luna, D. Dodt, P. De Vries, R. Felton, E. Giovanozzi, J. Harling, D. Harting, N. Hawkes, J. Hobirk, I. Jenkins, E. Joffrin, M. Kempenaars, M. Lehnen, T. Loarer, P. Lomas, J. Mailloux, D. McDonald, a. Meigs, P. Morgan, I. Nunes, C. Perez van Thun, V. Riccardo, F. Rimini, a. Sirinnelli, M. Stamp, and I. Voitsekhovitch. Integration of a radiative divertor for heat load control into JET high triangularity ELMy H-mode plasmas. *Nuclear Fusion*, 52(6):063022, June 2012.

[4] M.N.A. Beurskens, J. Schweinzer, C. Angioni, A. Burckhart, C.D. Challis, I. Chapman, R. Fischer, J. Flanagan, L. Frassinetti, C. Giroud, J. Hobirk, E. Joffrin, A. Kallenbach, M. Kempenaars, M. Leyland, P. Lomas, G. Maddison, M. Maslov, R. McDermott, R. Neu, I. Nunes, T. Osborne, F. Ryter, S. Saarelma, P.A. Schneider, P. Snyder, G. Tardini, E. Viezzer, and E. Wolfrum. The effect of a metal wall on confinement in JET and ASDEX Upgrade. *Plasma Physics and Controlled Fusion*, 55(12):124043, December 2013.

[5] M.L. Reinke, J.W. Hughes, a. Loarte, D. Brunner, I.H. Hutchinson, B. LaBombard, J. Payne, and J.L. Terry. Effect of N2, Ne and Ar seeding on Alcator C-Mod H-mode confinement. *Journal of Nuclear Materials*, 415(1):S340–S344, August 2011.

[6] G Tardini, R Fischer, F Jenko, a Kallenbach, R M McDermott, T Pütterich, S K Rathgeber, M Schneller, J Schweinzer, a C C Sips, D Told, and E Wolfrum. Core transport analysis of nitrogen seeded H-mode discharges in the ASDEX Upgrade. *Plasma Physics and Controlled Fusion*, 55(1):015010, January 2013.

[7] H.R. Wilson, S.C. Cowley, A. Kirk, and P.B. Snyder. Magneto-hydrodynamic stability of the H-mode transport barrier as a model for edge localized modes: an overview. *Plasma Physics and Controlled Fusion*, 48(5A):A71–A84, May 2006.

[8] P.B. Snyder, N. Aiba, M. Beurskens, R.J. Groebner, L.D. Horton, a.E. Hubbard, J.W. Hughes, G.T.a. Huysmans, Y. Kamada, a. Kirk, C. Konz, a.W. Leonard, J. Lönnroth, C.F. Maggi, R. Maingi, T.H. Osborne, N. Oyama, a. Pankin, S. Saarelma, G. Saibene, J.L. Terry, H. Urano, and H.R. Wilson. Pedestal stability comparison and ITER pedestal prediction. *Nuclear Fusion*, 49(8):085035, August 2009.

[9] A Kallenbach, R Dux, J C Fuchs, R Fischer, B Geiger, L Giannone, A Herrmann, T Lunt, V Mertens, R McDermott, R Neu, T Pütterich, S Rathgeber, V Rohde, K Schmid, J Schweinzer,

and W Treutterer. Divertor power load feedback with nitrogen seeding in ASDEX Upgrade. *Plasma Physics and Controlled Fusion*, 52(5):055002, May 2010.

[10] E Viezzer, T Pütterich, R Dux, and R M McDermott. High-resolution charge exchange measurements at ASDEX Upgrade. *The Review of scientific instruments*, 83(10):103501, October 2012.

[11] S.K. Rathgeber, L. Barrera, T. Eich, R. Fischer, B. Nold, W. Suttrop, M. Willensdorfer, E. Wolfrum, and ASDEX Upgrade Team. Estimation of edge electron temperature pro les via forward modelling of the electron cyclotron radiation transport at ASDEX Upgrade. *Plasma Physics and Controlled Fusion*, 2012.

[12] H. Murmann, S. Gotsch, H. Rohr, H. Salzmann, and K. H. Steuer. The Thomson scattering systems of the ASDEX upgrade tokamak. *Review of Scientific Instruments*, 63(10):4941, 1992.

[13] B. Kurzan and H.D. Murmann. Edge and core Thomson scattering systems and their calibration on the ASDEX Upgrade tokamak. *The Review of scientific instruments*, 82(10):103501, October 2011.

[14] E. Wolfrum, F. Aumayr, D. Wutte, Hp. Winter, E. Hintz, D. Rusbuldt, and R. P. Schorn. Fast lithium-beam spectroscopy of tokamak edge plasmas. *Review of Scientific Instruments*, 64(8):2285, 1993.

[15] R. Fischer, E. Wolfrum, and J. Schweinzer. Probabilistic lithium beam data analysis. *Plasma Physics and Controlled Fusion*, 50(8):085009, August 2008.

[16] O. Gehre. The HCN-laser-interferometer of the divertor tokamak ASDEX. *International Journal of Infrared and Millimeter Waves*, 5(3):369–379, March 1984.

[17] R Fischer, C J Fuchs, B Kurzan, W Suttrop, E Wolfrum, and The ASDEX Upgrade Team. Integrated data analysis of profile diagnostics at ASDEX Upgrade. *Fusion Science and Technology*, 58(2):675–684, 2010.

[18] C. Angioni, H. Weisen, O.J.W.F. Kardaun, M. Maslov, a. Zabolotsky, C. Fuchs, L. Garzotti, C. Giroud, B. Kurzan, P. Mantica, a.G. Peeters, and J. Stober. Scaling of density peaking in H-mode plasmas based on a combined database of AUG and JET observations. *Nuclear Fusion*, 47(9):1326–1335, September 2007.

[19] G. Saibene, R. Sartori, A. Loarte, D.J. Campbell, P.J. Lomas, V. Parail, K.D. Zastrow, Y. Andrew, S. Sharapov, A. Korotkov, M. Becoulet, G.T.A. Huysmans, H.R. Koslowski, R. Budny, G.D. Conway, J. Stober, W. Suttrop, A. Kallenbach, M. von Hellermann, and M.N.A. Beurskens. Improved performance of ELMy H-modes at high density by plasma shaping in JET. *Plasma Physics and Controlled Fusion*, 44:1769–1799, 2002.

[20] C Giroud, S Jachmich, P Jacquet, a Järvinen, E Lerche, F Rimini, L Aho-Mantila, N Aiba, I Balboa, P Belo, C Angioni, M Beurskens, S Brezinsek, F J Casson, I Coffey, G Cunningham, E Delabie, S Devaux, P Drewelow, L Frassinetti, a Figueiredo, a Huber, J Hillesheim, L Garzotti, M Goniche, M Groth, Hyun-Tae Kim, M Leyland, P Lomas, G Maddison, S Marsen, G Matthews, a Meigs, S Menmuir, T Puetterich, G van Rooij, S Saarelma, M Stamp, H Urano, and a Webster. Progress at JET in integrating ITER-relevant core and edge plasmas within the constraints of an ITER-like wall. *Plasma Physics and Controlled Fusion*, 57(3):035004, March 2015.

[21] M.N.A. Beurskens, M.G. Dunne, and L. Frassinetti. Comparison of nitrogen and carbon impurity seeding in AUG. In *42nd EPS Conference on Plasma Physics*, Lisbon, 2015.

[22] C.D. Challis, J. Garcia, M. Beurskens, P. Buratti, E. Delabie, P. Drewelow, L. Frassinetti, C. Giroud, N. Hawkes, J. Hobirk, E. Joffrin, D. Keeling, D.B. King, C.F. Maggi, J. Mailloux, C. Marchetto, D. McDonald, I. Nunes, G. Pucella, S. Saarelma, and J. Simpson. Improved confinement in JET high β plasmas with an ITER-like wall. *Nuclear Fusion*, 55(5):053031, May 2015.

[23] C Konz, W Zwingmann, F Osmanlic, B Guillerminet, F Imbeaux, and P Huynh. First physics applications of the Integrated Tokamak Modelling (ITM-TF) tools to the MHD stability analysis of experimental data and ITER scenarios. In *EPS, Strasbourg*, 2011.

[24] GTA Huysmans, J.P Goedbloed, and W Kerner. Helena. In *Conference on computational plasma physics (CP90)*, page 371, 1991.

[25] A. B. Mikhailovskii, G. T. A. Huijsmans, S. E. Sharapov, and W. Kerner. No Title. *Plasma Physics Reports*, 23:844, 1997.

[26] P.J. McCarthy. Analytical solutions to the GradShafranov equation for tokamak equilibrium with dissimilar source functions. *Physics of Plasmas*, 6(9):3554, 1999.

[27] P.J. McCarthy. Identification of edge-localized moments of the current density profile in a tokamak equilibrium from external magnetic measurements. *Plasma Physics and Controlled Fusion*, 54(1):015010, January 2012.

[28] M.G. Dunne, P.J. McCarthy, E. Wolfrum, R. Fischer, L. Giannone, and a. Burckhart. Measurement of neoclassically predicted edge current density at ASDEX Upgrade. *Nuclear Fusion*, 52(12):123014, December 2012.

[29] M.G. Dunne, S. Rathgeber, A. Burckhart, R. Fischer, L. Giannone, P.J. McCarthy, P.a. Schneider, and E. Wolfrum. Impact of Te and ne on edge current density profiles in ELM mitigated regimes on ASDEX Upgrade. *Nuclear Fusion*, 55(1):013013, January 2015.

[30] P.B. Snyder, R.J. Groebner, J.W. Hughes, T.H. Osborne, M. Beurskens, a.W. Leonard, H.R. Wilson, X.Q. Xu, Home Search, Collections Journals, About Contact, My Iopscience, and I P Address. A first-principles predictive model of the pedestal height and width: development, testing and ITER optimization with the EPED model. *Nuclear Fusion*, 51(10):103016, October 2011.

[31] M. N. a. Beurskens, T. H. Osborne, P. a. Schneider, E. Wolfrum, L. Frassinetti, R. Groebner, P. Lomas, I. Nunes, S. Saarelma, R. Scannell, P. B. Snyder, D. Zarzoso, I. Balboa, B. Bray, M. Brix, J. Flanagan, C. Giroud, E. Giovannozzi, M. Kempenaars, a. Loarte, E. de la Luna, G. Maddison, C. F. Maggi, D. McDonald, R. Pasqualotto, G. Saibene, R. Sartori, E. Solano, M. Walsh, and L. Zabeo. H-mode pedestal scaling in DIII-D, ASDEX Upgrade, and JET. *Physics of Plasmas*, 18(5):056120, 2011.

[32] S. Saarelma, A. Järvinen, M. Beurskens, C. Challis, L. Frassinetti, C. Giroud, M. Groth, M. Leyland, C. Maggi, and J. Simpson. The effects of impurities and core pressure on pedestal stability in Joint European Torus (JET). *Physics of Plasmas*, 22(5):056115, May 2015.

[33] Mike G Dunne. Predictive modelling of the impact of a radiative divertor on pedestal confinement on ASDEX Upgrade. In *57th Annual Meeting of the APS Division of Plasma physics*, Savannah, GA, 2015.

[34] T.H. Osborne, G.L. Jackson, Z. Yan, R. Maingi, D.K. Mansfield, B.a. Grierson, C.P. Chrobak, a.G. McLean, S.L. Allen, D.J. Battaglia, a.R. Briesemeister, M.E. Fenstermacher, G.R. McKee, and P.B. Snyder. Enhanced H-mode pedestals with lithium injection in DIII-D. *Nuclear Fusion*, 55(6):063018, June 2015.

[35] A. Burckhart, E. Wolfrum, R. Fischer, K. Lackner, and H. Zohm. Inter-ELM behaviour of the electron density and temperature pedestal in ASDEX Upgrade. *Plasma Physics and Controlled Fusion*, 52(10):105010, October 2010.

[36] F. Sommer, J. Stober, C. Angioni, E. Fable, M. Bernert, a. Burckhart, V. Bobkov, R. Fischer, C. Fuchs, R.M. McDermott, W. Suttrop, and E. Viezzer. Transport properties of H-mode plasmas with dominant electron heating in comparison to dominant ion heating at ASDEX Upgrade. *Nuclear Fusion*, 55(3):033006, March 2015.

[37] E Viezzer, T Pütterich, E Fable, a Bergmann, R Dux, R M McDermott, R M Churchill, and M G Dunne. Rotation and density asymmetries in the presence of large poloidal impurity flows in the edge pedestal. *Plasma Physics and Controlled Fusion*, 55(12):124037, December 2013.